PHYSICAL REVIEW E **99**, 033116 (2019)

Turbulent convection and large scale circulation in a cube with rough horizontal surfaces

N. Foroozani,[1,2] J. J. Niemela,[1] V. Armenio,[2] and K. R. Sreenivasan[3]
[1]*International Centre for Theoretical Physics, Strada Costiera 11, 34151 Trieste, Italy*
[2]*Dipartimento di Ingegneria e Architettura, Università di Trieste, 34127 Trieste, Italy*
[3]*Departments of Physics and Mechanical and Aerospace Engineering, and the Courant Institute of Mathematical Sciences, New York University, New York, New York 10012 USA*

(Received 9 July 2018; revised manuscript received 3 February 2019; published 28 March 2019)

Large-eddy simulations of thermal convection are presented and discussed for a cube with rough horizontal surfaces. Two types of roughness are considered: uniformly placed pyramids, and grooves aligned parallel to one set of sidewalls. The Rayleigh number is 10^8, the Prandtl number 0.7, and the aspect ratio 1, as in a previous study [N. Foroozani, J. J. Niemela, V. Armenio, and K. R. Sreenivasan, Phys. Rev. E **95**, 033107 (2017)], except that the meshes here are finer. When the thermal boundary layers are sufficiently large relative to the characteristic roughness height, i.e., for hydrodynamically smooth conditions, the mean properties of the large scale circulation (LSC) are qualitatively similar to the case of smooth surfaces. In particular, the LSC is always aligned along one of the diagonals of the cube. When the boundaries are hydrodynamically rough, the same result holds true only for the case of pyramidal structures; for grooved surfaces, the LSC is forced to be parallel to the sidewalls on average, alternating rapidly between the two diagonals of the cube with a mean period of the order 10 turnover times. Our analysis suggests that the difference from the pyramidal case is due to the breaking of the horizontal x-z symmetry under conditions of hydrodynamical roughness, and the corresponding directional concentration of plume emission along the grooves, from which the LSC is generated, providing a strong restoring force. Furthermore, in this study we observed a small reduction in heat transport for both roughness configurations which is in good agreement with past studies.

DOI: 10.1103/PhysRevE.99.033116

I. INTRODUCTION

Turbulent Rayleigh-Bénard convection (RBC) in a container with aspect ratio $\Gamma = L/H \sim O(1)$ (where L and H are the characteristic horizontal and vertical length scales, respectively) exhibits a strong large scale circulation (LSC), also known as the "mean wind," regardless of the shape of the container, with upward and downward flows on opposite plates of the cell [1–19]. This structure typically undergoes nonperiodic changes in its lateral orientation; in a cubic confinement it has eight states open to it (see [1,20,21]): two diagonals times two directions of flow, plus four transient states aligned with the sidewalls. Also, flow reversal (cessation of the LSC in one direction and restarting in the opposite one) has been observed to occur in different geometrical configurations (for a comprehensive explanation of flow reversals we refer to Verma [22]).

Since the flow is long-term unstable in any one of the states, we define "transient" orientations as those with lifetimes of the order of one turnover time (the minimum timescale for the LSC). For a given value of the Prandtl number $\mathrm{Pr} = \nu/\kappa$ (where ν and κ are the kinematic viscosity and thermal diffusivity of the fluid, respectively) the LSC is robust over a range of the Rayleigh number [23] $\mathrm{Ra} = \alpha g \Delta T H^3/\nu\kappa$, where g is the gravitational acceleration, α the thermal expansion coefficient of the fluid, and ΔT the temperature difference across the fluid layer of depth H. For asymptotically large Ra, turbulent velocity fluctuations presumably become comparable to the mean wind rendering the LSC ill defined [12]. It is known that the LSC dynamics alters with the boundary shape, as the observations in upright cylindrical cells [24,25], horizontal cylindrical cell [26], rectangular cells [4] differ. For instance, Zhou *et al.* [4] found in their horizontal cylinder of $\Gamma \sim O(1)$, the LSC orient along the longest diagonals of the cell and it switches periodically between diagonals which can be explained using the Brown and Ahlers [27,28] model. This model consists of stochastic ordinary differential equations in which turbulent fluctuations drive motion a cell-geometry-dependent potential, which controls the dynamics of the LSC orientation.

Typically, idealized smooth heating and cooling plates have been used to reduce the number of free parameters but surface roughness is present in many realistic flows and its effects are nontrivial; indeed, turbulent flows over rough walls are critical in engineering and geophysics (e.g., heat exchangers, urban atmospheric boundary, ocean convection, etc.). Previous theoretical [29,30], experimental [31–33], and numerical [34–39] studies have addressed different aspects of the problem, but one of their main concerns has usually been the scaling law of heat transport Nu as a function of Ra for various roughness heights (k) and shapes. Different roughness shapes have been studied, e.g., bars [35,40,41], cubes [42–44], spheres [45], grooves [32,34,46], and pyramids [31,47–49].

More specifically, in their experiments, Du and Tong [47,50] studied the effect of roughness in RBC in cylindrical cells filled with water and having aspect ratios $\Gamma = 0.5$ and 1. They used pyramidal roughness elements, distributed over the top and bottom plates, and observed an enhancement of plume emission from the tips of the pyramids. Specifically, the interaction between the horizontal shear flow due to the

LSC and the ordered rough surface created a secondary flow in the interstitial regions consisting of an eddy with vorticity opposing the LSC. This secondary flow, together with the LSC, facilitated the detachment of the thermal boundary layer near the tips of the pyramids. Other laboratory experiments of Shen *et al.* [31] and Qiu *et al.* [48] also report the enhancement of plume emission by 20%–76%, respectively.

Numerical simulations of Stringano *et al.* [34] employed the same geometry but with V-shaped grooves instead of pyramids. Over a total range of Ra from 2×10^6 to 2×10^{11}, they observed an increase of heat transfer for $\mathrm{Ra} > \mathrm{Ra}_{th} = 10^8$, where Ra_{th} refers to a threshold value of Ra at which the estimated thermal boundary layer height becomes smaller than the characteristic roughness height. They demonstrated that the secondary flow trapped between the grooves would lift up the boundary layers. Also, in agreement with Du and Tong [50], the authors showed that the presence of roughness on the plate surface dramatically changed the plume emission and, consequently, the heat transfer rate; the latter because the presence of grooves favors flow separation at the sharp edges both enhancing the generation of plumes and fixing the location of their emission.

In two-dimensional (2D) and three-dimensional (3D) direct numerical simulations (DNS) of Wagner and Shishkina [35,41], four box-shaped obstacles were attached to the heating and the cooling plates. Aside from varying Ra, they varied the height and width of the obstacles. These authors also observed secondary rolls to appear occasionally between the isothermal roughness elements, resulting in heat-transport enhancement in some cases, although the interstitial fluid tended to stagnate and impede the heat transfer for sufficiently small distances between the roughness elements. This was seen as well in recent simulations of Zhang *et al.* [46] who found that roughness elements do not always lead to an increase in Nu. Their simulations were carried out over a range of Rayleigh numbers up to $\mathrm{Ra} = 10^{11}$ in 2D and at $\mathrm{Ra} = 10^8$ in 3D. Among other quantities, these authors computed the ratio $\mathrm{Nu}(k)/\mathrm{Nu}(0)$ as a function of the normalized roughness height k/k_{th}^0, where $k_{th}^0 = 1/[2\mathrm{Nu}(0)]$ is the estimated thickness of thermal boundary layer (BL) for a smooth horizontal surface (taking $H = 1$), and Nu(0) is the corresponding Nusselt number. This was done for both 2D and 3D cases. They identified two regimes for $\mathrm{Nu}(k)$ with either enhancement or reduction of the heat transfer; specifically, in the 3D case, Nu, normalized by its smooth surface value, was shown to decrease by a maximum of 5% for $k/k_{th}^0 < 2.5$. This decrease was attributed to the presence of low speed recirculation within the asperities, creating a barrier against heat transport.

It should be noted that the term “roughness” is usually used to describe elements that protrude beyond the velocity and thermal BLs. This is different from the more prescriptive view [51] that a boundary behaves as rough when the blockage ratio k_v/k of the viscous boundary layer thickness to the roughness height is of the order of 40. When the Prandtl number $0.7 \leqslant \mathrm{Pr} \leqslant 5$, k_{th} and k_v are of the same order of magnitude and the condition $k_v/k \geqslant 40$ does not apply either in experimental studies or numerical simulations. This is the reason why some authors prefer to use the words “grooves” or “obstacles” instead of “rough” [34,41]. In this paper, we use the term *hydrodynamically rough* to highlight the similarities to the other RBC studies.

To the best of our knowledge, there are relatively few studies that examine the influence of roughness on properties of the LSC in the confined geometries. This is the focus of this study. Furthermore, instead of the usual cylindrical containers, we consider a cubic geometry that places some restrictions on the directionality of the lateral flow. Among all the possible roughness configurations, we consider two archetypal types: (a) a pyramidal shape distributed uniformly on the horizontal plates, and (b) V-shaped grooves set parallel to one set of sidewalls so that a specific (and unstable) direction for the LSC is preferentially set in the cell. As regards the effect of roughness on Nu, this study complements the recent findings of Zhang *et al.* [46] which will be briefly discussed below.

II. NUMERICAL METHODS

The numerical method is essentially the same as Foroozani *et al.* [1,19] where more details are described, except for improved resolution. Here, we repeat some of the salient features. Large-eddy simulations of the Boussinesq form of the Navier-Stokes equations for incompressible flow were performed using a second-order nonstaggered fractional step method. Variables are filtered through application of a low-pass filter whose width is proportional to the cell size $\bar{\Delta} = (\Delta_x \Delta_y \Delta_z)^{1/3}$. The filtered governing equations can be written as follows:

$$\frac{\partial \bar{u}_j}{\partial x_j} = 0, \tag{1}$$

$$\frac{\partial \bar{u}_i}{\partial t} + \frac{\partial \bar{u}_j \bar{u}_i}{\partial x_j} = -\frac{1}{\rho_0}\frac{\partial \bar{p}}{\partial x_i} + \nu \frac{\partial^2 \bar{u}_i}{\partial x_j \partial x_j} - \frac{\bar{\rho}}{\rho_0} g \delta_{i2} - \frac{\partial \tau_{ij}}{\partial x_j}, \tag{2}$$

$$\frac{\partial \bar{\rho}}{\partial t} + \frac{\partial \bar{u}_j \bar{\rho}}{\partial x_j} = k \frac{\partial^2 \bar{\rho}}{\partial x_j \partial x_j} - \frac{\partial \lambda_j}{\partial x_j}. \tag{3}$$

Here, the symbol “bar” represents the filtering operation, u_i is the velocity component along the x_i direction (hereafter we also use u, v, and w along x, y, and z directions, respectively). The axis $x_2 \equiv y$ is vertical pointing upward, p is the hydrodynamic pressure, t is time, δ_{ij} is the Kronecker symbol, τ_{ij} and λ_j are the subgrid-scale (SGS) stress tensor and the SGS density flux, respectively. We assume that the density is a linear function of temperature as $\rho = \rho_0[1 - \alpha(T - T_0)]$, where ρ_0 is the density at the reference temperature T_0. Since we solve the turbulent field down to the wall, no-slip conditions are used at solid surfaces for the velocity; for the thermal field, adiabatic conditions are used at the vertical walls ($\partial \bar{\rho}/\partial \mathbf{n} = 0$, where $\mathbf{n}$ is the normal vector on surface) and isothermal conditions on the horizontal plates. A description of the method and of the SGS dynamic model is contained in [52,53]. The algorithm [54] has been extensively validated in Cartesian (and non-Cartesian) geometric configurations (see for a review Ref. [55]).

The variables are made nondimensional by choosing $H^* = H - 2k$, tip-to-tip distance, as the length scale, $U_f = \sqrt{\alpha g \Delta T H^*}$ as the velocity scale, and $\Delta\rho = \rho_t - \rho_b$ the density difference between the top and bottom plates, as the density scale. The eddy turnover time can be defined as $T_{\mathrm{eddy}} = 2H^*/v_{\mathrm{rms}}$ where v_{rms} is time average of the 16 probes at

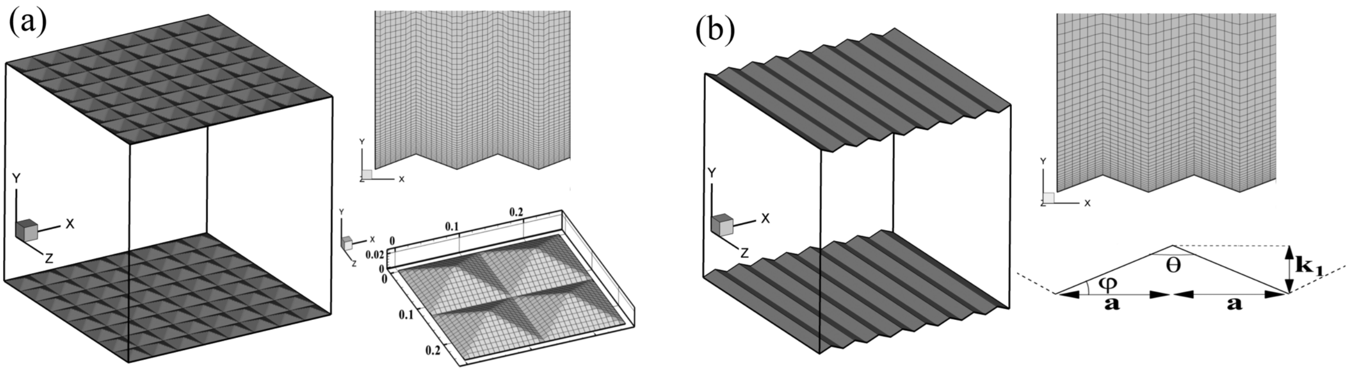

FIG. 1. (a) Pyramidal rough surfaces with $k_1 = 0.025H$. A 3D structure of a zoomed area is also shown $0 \leqslant x, z \leqslant 0.25$ and $0 \leqslant y \leqslant 0.025$; (b) 3D plot of grooved surface with height k_1. We studied three different heights with $k_1 = 0.025H,\ k_2 = 0.0125H$, and $k_3 = 0.00625H$; the geometry of roughness is constant in all cases with $2a = 0.125H$ [see the sketch in (b)]. Examples of stretched mesh along the y axis are shown to the right of (b).

midheight $(1/16)\sum_{i=1}^{16}(v_{\mathrm{rms}}^i)$ with $v_{\mathrm{rms}}^i(\mathbf{x}) = [\langle v(\mathbf{x})v(\mathbf{x})\rangle_t - \langle v(\mathbf{x})\rangle_t\langle v(\mathbf{x})\rangle_t]^{1/2}$; see [56].

Our large-eddy simulations enable comparisons with previous results [34,46,49,50]; we set the nominal Rayleigh number (based on H) to be $\mathrm{Ra} = 10^8$, $\mathrm{Pr} = 0.7$, and $\Gamma = 1$ in all present simulations. We apply two different roughness shapes on top and bottom plates: (a) a 64-pyramidal structure distributed uniformly over the plates with height $k_1 = 0.025H$ without a preferred orientation and (b) an 8-grooved plate with three different heights $k_1 = 0.025H$, $k_2 = 0.0125H$, and $k_3 = 0.00625H$ aligned with two side walls. Figures 1(a) and 1(b) show the convection cell and also the grid refinement for the pyramids and groove asperities. Note that the Rayleigh number using H^* instead of H is reduced slightly to 0.87×10^8 for the largest asperity. Although RB convection in cubic cells at $\mathrm{Ra} = 10^8$ is presently quite accessible with DNS, we decided to use large-eddy simulation (LES) because of the need to run very long-time simulations in order to elucidate the reorientation phenomena of the mean wind subject to roughness types having similar geometry but either full or broken x-z horizontal symmetry. Our simulations were run for over 700 large-eddy turnover times, and Nusselt numbers were computed for some 100 of them, always when conditions were statistically stabilized. It would be clearly very expensive for DNS to span similarly large calculations because of the CPU time required for each time iteration and the limitations in the time step.

As discussed above, the numerical algorithm has been validated in a number of cases. Moreover, as for the case of RB convection in cubic cells, validation tests were carried out in the case of smooth plates at different values of Ra, making comparisons with reference DNS data. Results of validation tests are shown in [19] (see Table 1 in that paper) and are not repeated here. We note that they underscore the ability of the present LES model to accurately predict the Nusselt number and flow field features for the grid resolutions used here.

We made considerable effort to generate smooth grids in rather complex geometries using curvilinear body-fitted meshes. Indeed, that was one of the challenges of this study. We used a hyperbolic tangent function to create the needed stretching [57] [see Eqs. (49)–(51)]. The stretching coefficient (C) is adjustable in our code. For instance, for the smooth wall $C = 0.0017$; for the roughness case k_1 it was slightly adjusted to $C = 0.002$. There are reasons for this adjustment; the stability of our numerical method is limited by the Courant-Friedrichs-Lewy (CFL) condition, where CFL is a function of grid spacing Δx, Δy, Δz. Therefore, in order to preserve the accuracy of the numerical method, we avoided highly skewed or irregular grids whenever possible. We made systematic tests and found that $C = 0.002$ is the best stretching factor, which also followed the accepted criteria for covering the boundary layers.

For the grooved and pyramidal plates, we have used, respectively, a grid size of $96 \times 96 \times 96$ and $128 \times 128 \times 128$. In the first case, we have placed eight grooves within the cell, while in the second case we considered 8×8 pyramids; therefore, the slant angle of asperities with height k_1 is $\varphi = 21.8^\circ$ and the tip angle is $\theta = 136.6^\circ$ [see Fig. 1(b)]. In all cases, the grid points are spaced equally in the horizontal directions (x, z), whereas they are stretched vertically close to the horizontal plates to solve appropriately the top and bottom boundary layers (see [58,59] for the relevant criteria which are satisfied here). The required number of grid points N_{BL} for solving the thermal boundary layer is listed in Table I, for each simulation. $\Delta_{\mathrm{min}}, y/H$ is the minimum nondimensional grid spacing, close to the top and bottom rough plates, and $\Delta_{\mathrm{max}}, y/H$ is the maximum nondimensional grid spacing at the cell center (see Table I). As in Foroozani *et al.* [1], to help enable statistical analysis and extract flow orientations in the cell, we placed 16 "numerical probes" in the midheight plane to record velocity time series. Figure 2 shows a schematic of the probe locations over the horizontal midplane. The azimuthal angle of each probe is given by $\phi_i = i\pi/8 \quad (i = 0, \dots, 15)$, and the distance from the vertical wall is $0.1H$ for all probes.

III. RESULTS AND DISCUSSION

In a previous work [1] we observed the orientation dynamics of the LSC in a cube with smooth plates. Briefly, under the same condition $\mathrm{Ra} = 10^8$, we observed that the LSC developed in a plane containing one of the diagonals of the cell and was stable for a period of time (which, on average, was much longer than the turnover time) before switching to

TABLE I. Simulation parameters for $\mathrm{Ra} = 10^8$, $\mathrm{Pr} = 0.7$, $\Gamma = 1$. The results for the smooth plates are from Foroozani *et al.* N_x, N_y, and N_z are the number of grid points along x, y, and z directions; $\Delta_{\min}, y$, $\Delta_{\max}, y$ are, respectively, the minimum and maximum grid spacing in the vertical direction y; N_{BL} is the number of grid points for solving the thermal boundary layer; the mean Nusselt number Nu represents the dimensionless heat transfer calculated over top and bottom horizontal planes near the boundary; and $T_{\mathrm{eddy}} = 2H^*/v_{rms}$ is the eddy turnover time of LSC.

Horizontal plates	$N_x \times N_y \times N_z$	k/H	$\Delta_{\min}, y/H$	$\Delta_{\max}, y/H$	N_{BL}	Nu	T_{eddy}	t/T_{eddy}
Smooth [1]	$64 \times 96 \times 64$		7.4×10^{-4}	2.2×10^{-2}	6	31.6	7	1200
Grooved	$96 \times 96 \times 96$	0.00625	2.145×10^{-3}	2.012×10^{-2}	6	31.46	4	940
Grooved	$96 \times 96 \times 96$	0.0125	2.157×10^{-3}	2.005×10^{-2}	6	31.11	5	690
Grooved	$96 \times 96 \times 96$	0.025	2.145×10^{-3}	1.995×10^{-2}	5	30.18	6	700
Pyramidal	$128 \times 128 \times 128$	0.025	1.968×10^{-3}	1.368×10^{-2}	5	30.46	6	360

the next adjacent corner, and so forth. These switches were not periodic in time, and between two stable flow configurations we observed transition states where the LSC was momentarily (of the order of one turnover time) parallel to one set of side walls. These transient flow states were also observed in later work by Giannakis [21]. In particular, the observation of these transient states allowed us to conclude that the preferred mode of orientational switching is a sweeping motion azimuthally connecting one stable state to its *nearest* neighboring stable state; in other words, we never observed switching in the same diagonal that would require a reversal of the vertical component of the mean velocity (although we cannot rule it out as a possibility without having sufficiently long time records). Flow reversal has been observed in recent DNS of 2D square cavities [60], but the results cannot be trivially extended to 3D flows, where 3D instabilities may dominate the dynamics. We note that in a recent archive paper Vasiliev *et al.* [61] propose a superposition of two orthogonal two-dimensional rolls where switching is suggested to result from the cessation of one of the roll pairs.

In this paper, we quantify our observations for a cubic container with rough top and bottom plates, through both time-averaged plots of the flow streamlines and measurements of the instantaneous velocity at various points in the horizontal midplane, as shown in Fig. 2. It should be noted that most of our focus in this part is for the roughness with (the largest) height k_1, unless otherwise stated.

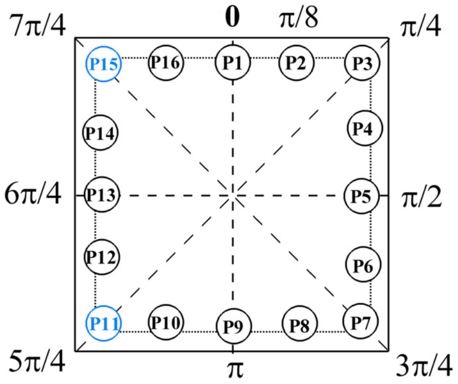

FIG. 2. Schematic of the horizontal midplane showing the azimuthal positions for probes, placed at azimuthal angles $\phi_i = (i\pi/8)$, $i = 0, \ldots, 15$. The distance from the vertical walls are $0.1H$ for all cases. In the case of grooves, the alignment is along the 0-π direction.

Figures 3(a) and 3(b) show time series of the normalized vertical velocity measurements for the case of hydrodynamically rough grooved surfaces (grooves with height k_1). Figure 3(a) shows signals recorded from probes P7 and P15 at the midheight corresponding to one particular diagonal (see Fig. 2). Similarly, Fig. 3(b) shows seemingly concurrent flow in an adjacent diagonal, with upflow at position P3 and downflow at P11. It is obviously not possible to have both flows occurring simultaneously. This scenario is profoundly different from that detected in [1], for which a velocity record

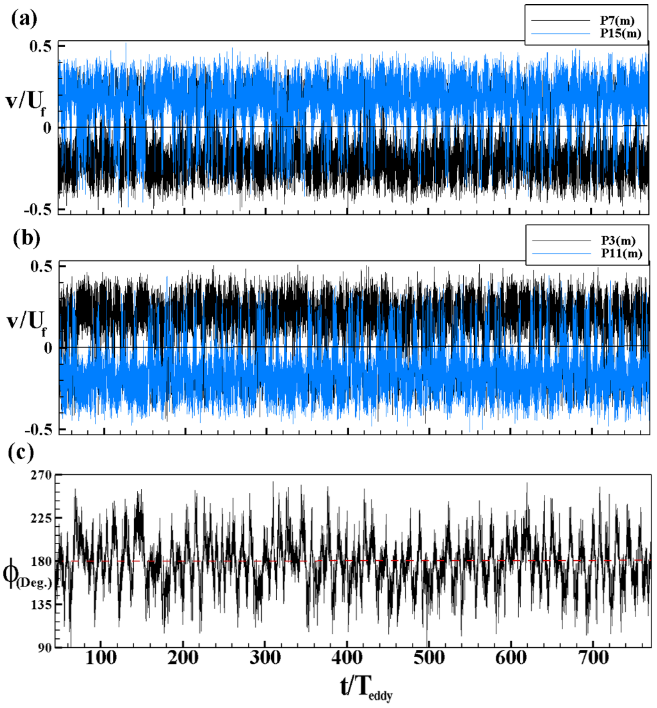

FIG. 3. Time series of the vertical velocity and its phase for different "probe" positions for grooved plate with $k_1 = 0.025$ (see Fig. 2 also). (a) Probes P7 and P15 at the midheight corresponding to the same diagonal. (b) Probes P3 and P11 at midheight in the opposite diagonal. (c) Time series of phase $\Phi(t)$ of the first Fourier mode of the vertical velocity used as an approximate measure for the time evolution of the orientation of the LSC, for $\mathrm{Ra} = 10^8$, $\mathrm{Pr} = 0.7$, and $\Gamma = 1$.

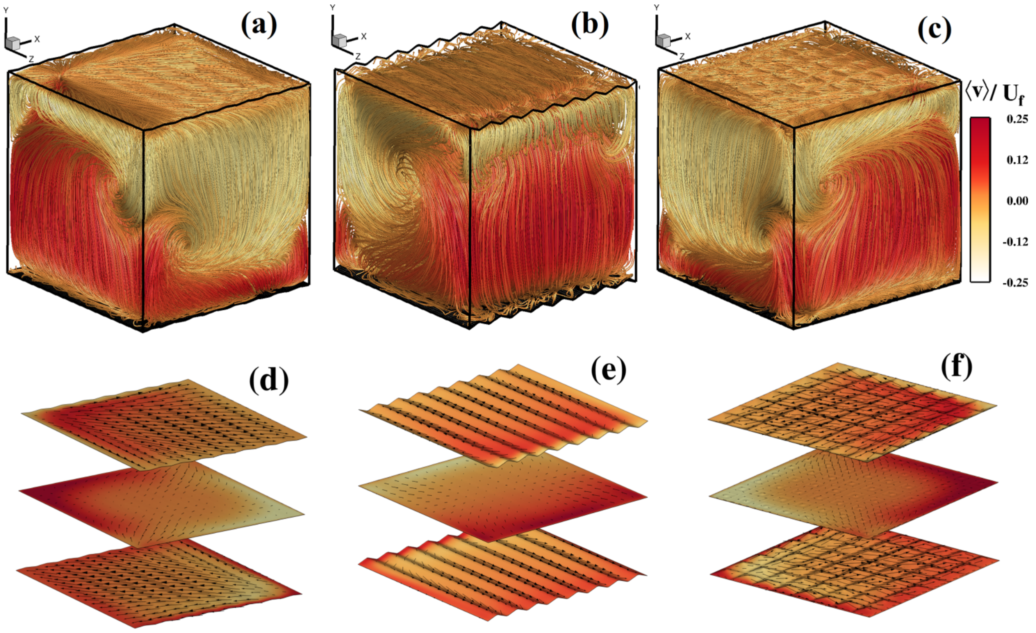

FIG. 4. Time-averaged velocity streamlines and velocity vectors in the cube with (a), (d) grooved plate with height $k_3 = 0.00625H$, (b), (e) grooved plate with height $k_1 = 0.025H$, and (c), (f) pyramidal roughness with $k_1 = 0.025H$ for $\mathrm{Ra} = 10^8$, $\mathrm{Pr} = 0.7$, and $\Gamma = 1$. The color coding depicts the magnitude of the vertical velocity normalized by the free fall velocity U_f. Note that the time averaging for (a) and (d) and (c) and (e) is for a period of time in which there are no major reorientations of the mean wind, for the purpose of reducing the effects of small turbulent fluctuations. In the case of (b) and (e), on the other hand, long-time averaging gives a representation of the mean orientation of the LSC which otherwise has large and rapid (compared to the averaging time) fluctuations in direction between adjacent diagonals. It serves to graphically illustrate the qualitative difference occurring when the mean wind interacts with roughness elements lacking x-z symmetry for boundaries that are furthermore hydrodynamically rough and, in particular, illustrate the time-averaged orientation of flow relative to the groove channels.

like that of Fig. 3(a) would be accompanied by an almost zero velocity record for the opposite diagonal plane over the same period of time [see also Fig. 4(b)].

In order to understand better the signal and its alignments, we computed at each time t the azimuthal Fourier transform of the vertical velocities $v_i(t)$ at a given probe, similar to Cioni *et al.* [62]. Thus, we obtain the phase $\Phi(t)$ and amplitude $M(t)$ of the dipolar mode. The first Fourier components A_1 and B_1 are given by

$$A_1(t) = \frac{1}{2}\sum_{j=1}^{16} v_i(t)\cos\phi_i, \;\; B_1(t) = \frac{1}{2}\sum_{j=1}^{16} v_i(t)\sin\phi_i, \qquad (4)$$

$$M(t) = \sqrt{A_1^2 + B_1^2}, \qquad \Phi(t) = \mathrm{sign}(B_1)\arccos\frac{A_1}{|\delta|}. \qquad (5)$$

Plotting the time series of the phase of the first Fourier mode $\Phi(t)$ of the vertical velocity for 16 probes [see Fig. 3(c)] shows that, on the average, the signal oscillates about the angle $\phi = 180^\circ$ where the change in phase $\Delta\phi$ is approximately confined to the range $225^\circ \leqslant \Delta\phi \leqslant 135^\circ$ corresponding to the adjacent corners of the cell. The resulting spectrum of the phase fluctuations in Fig. 3(c) is broadband with a weak peak corresponding to a sweeping period of the LSC between adjacent corners of roughly 10-LSC turnover times, as can also be discerned easily by visual inspection of the time series. A more detailed analysis would benefit from substantially longer time series. In particular, we do not find any long-time stable configuration of the LSC in the case of grooved surfaces under hydrodynamically rough conditions. Clearly, averaging over very long times will show a flow parallel to the corresponding set of sidewalls. We also found that the LSC maintains its strength $M(t) \neq 0$ with changes in azimuthal orientation. The oscillatory behavior noted above is not present when the estimated thermal boundary layer thickness is sufficiently large so that $k < k_{th}$, as we would expect, nor is it observed under any conditions of the pyramidal roughness.

The relevant difference between the two roughness types is that the grooves break the x-z symmetry and provide a preferred directionality whereas the pyramids do not. As a consequence, the grooves force the flow initially parallel to their direction due to the enhanced emission of the plumes along the sharp edges. As the flow adjusts to a stable diagonal direction, continued plume initialization pulls the LSC again parallel to the grooves, and its inertia causes it to overshoot and occupy the other diagonal. This process repeats itself indefinitely, yielding a continual oscillation about the mean direction parallel to the sidewalls.

Previous studies also show that the spatial or temporal symmetry of the system can be broken by an external field [63,64], i.e., applying a horizontal magnetic field enables to make the flow more and more 2D by inhibiting velocity gradients along the the direction of magnetic field. Gallet *et al.* [63] used cubic container filled with mercury Pr($\simeq$0.025) and observed the square symmetry can be broken applying a horizontal magnetic field, i.e., more complex mixed states are involved in the reversal process.

Streamlines averaged over times that are long compared to the turnover time are shown in the following: Fig. 4(a) shows the pattern for the grooved plates in the hydrodynamically smooth regime; Fig. 4(b) for the grooved plates in the hydrodynamically rough regime (height k_1); and Fig. 4(c) for the pyramidal plates with height k_1. The corresponding horizontal velocity vectors are in Figs. 4(d)–4(f). The color contour denotes the magnitude of the time-averaged vertical velocity $\langle v \rangle$ normalized by U_f. Figures 4(a) and 4(d) depict the flow structure over grooved plate with height k_3, which should be hydrodynamically smooth. The LSC is in a diagonal plane as it would be in the case of smooth boundaries; in this case, the roughness height is smaller than both thermal and viscous boundary layer thicknesses and therefore the boundary layers are not exposed to the mean wind. The same behavior is observed for the roughness height k_2.

Figures 4(b) and 4(e) and 4(c) and 4(f), on the other hand, present the flow structure over rough boundaries with height k_1 for grooves and pyramids, respectively, in which the system can be considered hydrodynamically rough. Examining the time-averaged streamlines and velocity vectors in Figs. 4(b) and 4(e), we see that the flow is instead parallel to the sidewalls, *on average*, although as we saw above it is rapidly oscillating between the two adjacent diagonals. This is consistent with taking the average of all phase values in Fig. 3(c) which gives a value of 180° [the red line in Fig. 3(c)] corresponding to a (time-averaged) flow between positions P1(m) and P9(m) (see Fig. 2). Time-averaged flow in a diagonal plane, however, is indeed observed when the pyramidal elements are hydrodynamically rough ($k > k_{th}$) [Figs. 4(c) and 4(f)], in contrast to a smoothed picture of the instantaneous flow over the averaging period. We might expect this result since there is no breaking of the x-z symmetry and therefore no preferential forcing in any direction, in contrast to the grooved cell.

Figure 5 shows the plume emission over the bottom plate for the grooves with $k_3 = 0.00625H$ and $k_1 = 0.025H$ height, respectively. The alignment of the LSC with the grooves may be due to different reasons. First, the grooves may behave as rails for the development of the boundary layer, in particular when their height is large enough to go out from the viscous part of the boundary layer; further, the look at the instantaneous plume emission for the grooves suggests that when their height is large enough, they provide an organization of the plume emission which appears aligned along the grooves and thus breaking the x-z symmetry.

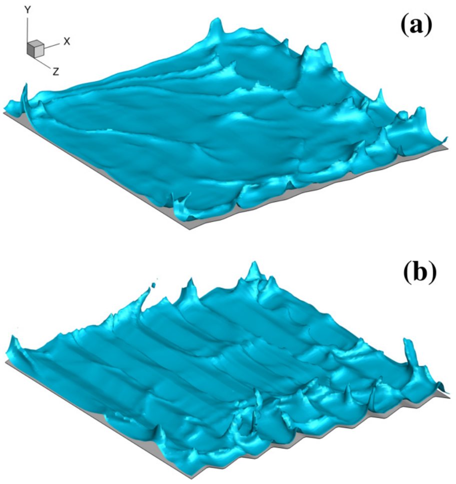

FIG. 5. Instantaneous normalized density isosurfaces over the bottom plate of the grooved surface with (a) height $k_3 = 0.00625H$, (b) height $k_1 = 0.025H$ for Ra $= 10^8$ and Pr $= 0.7$.

The changes of flow topology discussed above have some implications for the overall Nusselt number, which quantifies the increase in effective thermal conductance compared to that of a quiescent fluid. We computed the Nu in different vertical positions as described in Foroozani *et al.* [1] and found that the variation of Nu(y) is smaller than 1.5%.

At Ra $= 10^8$, we observe a slight decrease of Nu with the normalized roughness height (see Table I). For grooves with height k_1, we also observed that Nu is slightly smaller than for the pyramidal case. This may be caused by the lack of fluid motion in the third direction, and the fact that the hot and cold plume is more easily accumulated inside the cavity region, as discussed above. Furthermore, similar to [46], the rough surfaces have concave geometry in all simulations, which would result in the reduction of Nu for the hydrodynamically smooth plates.

In connection with [46], Nu was observed to decrease when $k/k_{th}^0 < 2.5$ with a maximum reduction of 6.3% for the 3D simulation at the same Ra $= 10^8$. In our 3D simulation, the height of roughness $0.3 \leqslant k/k_{th}^0 \leqslant 1.5$ resulted in a maximum reduction of Nu to be 3.6% for the pyramidal roughness with $k_1 = 0.025H$, and 4.5% for the grooved roughness with $k_3 = 0.00625H$, in good agreement with [46].

As already argued in [46], the reduction of the Nu has to be attributed to the fact that, under certain conditions, trapped hot fluid between the obstacles cannot be well mixed; i.e., the flow in the bulk cannot penetrate into the cavity regions, correspondingly impeding the global heat transport through the system. This is not the case for the grooved roughness in the hydrodynamically rough regime. In fact, there is a substantial difference between the flow studied in Zhang *et al.* [46] and our geometrical configuration. Zhang *et al.* [46] studied mostly idealized 2D flows, with the mean wind orthogonal to the rough elements. The conditions studied in that paper are mostly met in forced convection where the wind direction is driven by an external cause and is independent of the orientation of the roughness elements. In our 3D simulations, the mean wind interacts with the roughness elements resulting in the variation of the wind direction. As a consequence, the depression of Nu is less accentuated than in the idealized simulations of [46], due to the alignment of the mean wind with the grooves and the development of a three-dimensional boundary layer. In the literature it is well established that a 3D boundary layer develops in the presence of longitudinal grooves, and that it is characterized by regions of secondary recirculation in the cross-stream plane (see [65] and literature cited therein). As discussed by Speziale [66] a sufficient condition for a secondary recirculation to develop is the imbalance of the normal Reynolds stresses in the cross-sectional plane. The term $\partial^2(\tau_{22} - \tau_{33})/\partial x_2 \partial x_3$, with τ_{ii}, which is the normal Reynolds stress in the i direction, produces mean vorticity in the x_1 direction of the flow. In the present convective case, an additional term contributes to

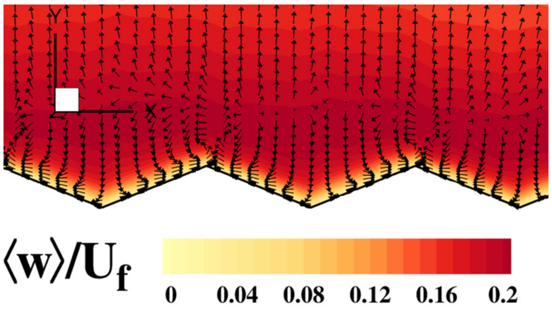

FIG. 6. Velocity vector on a vertical section over grooves with height k_1. Color contour denotes time-averaged streamwise velocity normalized by the free fall velocity $\langle w\rangle/U_f$ at $\mathrm{Ra}=10^8$, $\mathrm{Pr}=0.7$, and $\Gamma=1$.

the generation of the secondary motion, namely, $g/\rho_0\partial\overline{\rho}/\partial x_3$. This can be proven easily from the transport equation of the mean vorticity along the groove direction. This mean flow structure is depicted in Fig. 6; specifically, it is along the canyon within the groove [see also Fig. 4(e)] and a couple of symmetric secondary low-speed recirculation regions develop in the cross-sectional plane. Under the conditions just described, a dramatic reduction of the Nusselt number is not expected, as the near-wall flow structure is very different from that described in [46].

IV. CONCLUSIONS

In summary, we have studied convection in a cubical cell of $\Gamma=1$ for four cases: two cases are relative to the horizontal surface roughness at the top and bottom of the cell having x-z symmetry, and two cases when it does not. We found that the large scale circulation orients itself along the diagonal for both roughness types when the boundaries are hydrodynamically smooth. This is expected and corresponds to the observations made previously in the same cell with ideally smooth boundaries [1]. This applies also when the boundaries are hydrodynamically rough but the roughness does not have a preferential direction; conversely, for grooved roughness, the breaking of the x-z symmetry and the subsequent directional forcing of the mean wind results in a *time-averaged* orientation of the LSC parallel to a set of sidewalls, although with rapid fluctuations of its orientation between the two adjacent corners. In this case, any long-time averaging does not represent a smooth version of the instantaneous flow but rather the time-averaged orientation of the mean flow which otherwise fluctuates rapidly in time (compared to the averaging time), and with relatively large amplitude. As shown in Fig. 4(b), the average orientation of the LSC being parallel to the groove channels leads to the inference that the stagnation regions in the hydrodynamically rough regime can be reduced substantially. Although only two kinds of organized rough structures have been investigated here, this study sheds light on the importance of roughness symmetry on the mean flow and complements the observations of heat transfer by Zhang *et al.* [46], which remains valid for cavities for which the mean wind is forced to stay parallel to side walls. In agreement with past studies, we observed a modest reduction in the heat transport for both roughness configurations.

ACKNOWLEDGMENTS

The authors are grateful to M. De Marchis for fruitful conversations and discussions. We acknowledge financial support by the Abdus Salam International Centre for Theoretical Physics (ICTP). The computations have been performed on the ARGO HPC facilities of ICTP in Trieste. This research received partial financial support from Fondo Europeo di Sviluppo Regionale/LUNES project, Grant No. POR FESR 2014-2020.

---

[1] N. Foroozani, J. J. Niemela, V. Armenio, and K. R. Sreenivasan, Phys. Rev. E **95**, 033107 (2017).
[2] G. Zocchi, E. Moses, and A. Libchaber, Phys. A (Amsterdam) **166**, 387 (1990).
[3] T. Haramina and A. Tilgner, Phys. Rev. E **69**, 056306 (2004).
[4] S.-Q. Zhou, C. Sun, and K.-Q. Xia, Phys. Rev. E **76**, 036301 (2007).
[5] R. Krishnamurthy and L. N. Howard, Proc. Natl. Acad. Sci. USA **78**, 1981 (1981).
[6] B. Castaing, G. Gunaratne, F. Heslot, L. Kadanoff, A. Libchaber, S. Thomae, X.-Z. Wu, S. Zaleski, and G. Zanetti, J. Fluid Mech. **204**, 1 (1989).
[7] M. Sano, X.-Z. Wu, and A. Libchaber, Phys. Rev A **40**, 6421 (1989).
[8] S. Ciliberto, S. Cioni, and C. Laroche, Phys. Rev. E **54**, R5901 (1996).
[9] X.- L Qiu and K.- Q Xia, Phys. Rev. E **58**, 486 (1998).
[10] J. J. Niemela, L. Skrbek, K. R. Sreenivasan, and R. J. Donnelly, Nature (London) **404**, 837 (2000).
[11] J. J. Niemela, L. Skrbek, K. R. Sreenivasan, and R. J. Donnelly, J. Fluid Mech. **449**, 169 (2001).
[12] K. R. Sreenivasan, A. Bershadskii, and J. J. Niemela, Phys. Rev. E **65**, 056306 (2002).
[13] Y. Tsuji, T. Mizuno, T. Mashiko, and M. Sano, Phys. Rev. Lett. **94**, 034501 (2005).
[14] Z. A. Daya and R. E. Ecke, Phys. Rev. Lett. **87**, 184501 (2001).
[15] O. Shishkina and C. Wagner, J. Fluid Mech. **599**, 383 (2008).
[16] J. Bailon-Cuba, M. S. Emran, and J. Schumacher, J. Fluid Mech. **655**, 152 (2010).
[17] F. Chillà and J. Schumacher, Eur. Phys. J. E **35**, 58 (2012).
[18] M. Kaczorowski and K. Q. Xia, J. Fluid Mech. **722**, 596 (2013).
[19] N. Foroozani, J. J. Niemela, V. Armenio, and K. R. Sreenivasan, Phy. Rev. E **90**, 063003 (2014).
[20] K. Bai, D. Ji, and E. Brown, Phys. Rev. E **93**, 023117 (2016).
[21] D. Giannakis, A. Kolchinskaya, D. Krasnov, and J. Schumacher, J. Fluid Mech. **847**, 735 (2018).
[22] M. K. Verma, *Physics of Buoyant Flows: From Instabilities to Turbulence* (World Scientific, Singapore, 2018).
[23] A. Vasiliev, A. Sukhanovskii, P. Frick, A. Budnikov, V. Fomichev, M. Bolshukhin, and R. Romanov, Int. J. Heat Mass Transfer **102**, 201 (2016).
[24] E. Brown and G. Ahlers, J. Fluid Mech. **568**, 351 (2006).

[25] H.-D. Xi, Q. Zhou, and K. Q. Xia, Phys. Rev. E **73**, 056312 (2006).

[26] H. Song, E. Brown, R. Hawkins, and P. Tong, J. Fluid Mech. **740**, 136 (2014).

[27] E. Brown and G. Ahlers, Phys. Fluids **20**, 105105 (2008).

[28] E. Brown and G. Ahlers, Phys. Fluids **20**, 075101 (2008).

[29] E. Villermaux, Phys. Rev. Lett. **81**, 4859 (1998).

[30] X. Zhu, R. J. A. M. Stevens, R. Verzicco, and D. Lohse, Phys. Rev. Lett. **119**, 154501 (2017).

[31] Y. Shen, P. Tong, and K.-Q. Xia, Phys. Rev. Lett. **76**, 908 (1996).

[32] P. E. Roche, B. Castaing, B. Chabaud, and B. Hébral, Phys. Rev. E **63**, 045303 (2001).

[33] J.-C. Tisserand, M. Creyssels, Y. Gasteuil, H. Pabiou, M. Gibert, B. Castaing, and F. Chillà, Phys. Fluids **23**, 015105 (2011).

[34] G. Stringano, G. Pascazio, and R. Verzicco, J. Fluid Mech. **557**, 307 (2006).

[35] O. Shishkina and C. Wagner, J. Fluid Mech. **686**, 568 (2011).

[36] S. Toppaladoddi, S. Succi, and J. S. Wettlaufer, Europhys. Lett. **111**, 44005 (2015).

[37] S. Toppaladoddi, S. Succi, and J. S. Wettlaufer, Procedia IUTAM **15**, 34 (2015).

[38] S. Toppaladoddi, S. Succi, and J. S. Wettlaufer, Phys. Rev. Lett. **118**, 074503 (2017).

[39] D. Goluskin and C. R. Doering, J. Fluid Mech. **804**, 370 (2016).

[40] J. Bailon-Cuba, O. Shishkina, C. Wagner, and J. Schumacher, Phys. Fluids **24**, 107101 (2012).

[41] S. Wagner and O. Shishkina, J. Fluid. Mech. **763**, 109 (2015).

[42] O. Liot, J. Salort, R. Kaiser, R. du Puits, and F. Chillà, J. Fluid Mech. **786**, 275 (2016).

[43] O. Liot, Q. Ehlinger, E. Rusaouën, T. Coudarchet, J. Salort, and F. Chillà, Phys. Rev. Fluids **2**, 044605 (2017).

[44] J. Salort, O. Liot, E. Rusaouen, F. Seychelles, J. C. Tisserand, M. Creyssels, B. Castaing, and F. Chillà, Phys. Fluids **26**, 015112 (2014).

[45] S. Ciliberto and C. Laroche, Phys. Rev. Lett. **82**, 3998 (1999).

[46] Y. Zhang, C. Sun, Y. Bao, and Q. Zhou, J. Fluid Mech. **836**, R2 (2018).

[47] Y.-B. Du and P. Tong, Phys. Rev. Lett **81**, 987 (1998).

[48] X.-L. Qiu, K.-Q. Xia, and P. Tong, J. Turbul. **6**, N30 (2005).

[49] P. Wei, T. S. Chan, R. Ni, X.-Z. Zhao and K.-Q. Xia, J. Fluid Mech. **740**, 28 (2014).

[50] B. Y. Du and P. Tong, J. Fluid Mech. **407**, 57 (2000).

[51] J. Jiménez, Annu. Rev. Fluid Mech. **36**, 173 (2004).

[52] V. Armenio and U. Piomelli, Flow Turbulence Combust. **65**, 51 (2000).

[53] V. Armenio and S. Sarkar, J. Fluid Mech. **459**, 1 (2002).

[54] Y. Zang, R. L. Street, and J. Koseff, J. Comput. Phys. **114**, 18 (1994).

[55] V. Armenio, J. Hydr. Eng. **143**, 03117007 (2017).

[56] P. K. Mishra, A. K. De, M. K. Verma, and V. Eswaran, J. Fluid Mech. **668**, 480 (2011).

[57] M. Vinokur, J. Comput. Phys. **50**, 215 (1983).

[58] R. Verzicco and R. Camussi, J. Fluid Mech. **477**, 19 (2003).

[59] O. Shishkina, Richard J. A. M. Stevens, S. Grossmann, and D. Lohse, New J. Phys. **12**, 075022 (2010).

[60] A. Castillo-Castellanos, A. Sergent, and M. Rossi, J. Fluid Mech. **808**, 614 (2016).

[61] A. Vasiliev, P. Frick, A. Kumar, R. Stepanov, A. Sukhanovskii, and M. K. Verma, arXiv:1805.06718.

[62] S. Cioni, S. Ciliberto, and J. Sommeria, J. Fluid Mech. **335**, 111 (1997).

[63] B. Gallet, J. Herault, C. Laroche, F. Pétrélis, and S. Fauve, Geophys. Astrophys. Fluid Dyn. **106**, 468 (2012).

[64] S. Fauve, C. Laroche, A. Libchaber, and B. Perrin, Phys. Rev. Lett **52**, 1774 (1984).

[65] L. Falcomer and V. Armenio, J. Turbulence **3**, N8 (2002).

[66] C. Speziale, J. Fluid Mech. **178**, 459 (1987).